Interfacial and bulk properties of hole transporting materials in perovskite solar cells: spiro-MeTAD versus spiro-OMeTAD

Xavier Sallenave, Mona Shasti, Elham Halvani Anaraki, Dmytro Volyniuk, Juozas Vidas Grazulevicius, Shaik M Zakeeruddin, Abdollah Mortezaali, Michael Grätzel, Anders Hagfeldt, Gjergji Sini

Interfacial and Bulk Properties of Hole Transporting Materials in Perovskite Solar Cells: Spiro-MeTAD versus Spiro-OMeTAD

Xavier Sallenave[1], Mona Shasti [2,3], Elham Halvani Anaraki[2], Dmytro Volyniuk[4] , Juozas Vidas Grazulevicius[4], Shaik M. Zakeeruddin[2], Abdollah Mortezaali[3], Michael Grätzel[2], Anders Hagfeldt [2]*, and Gjergji Sini[1]**

[1] Laboratoire de Physicochimie des Polymères et des Interfaces, EA 2528 Université de Cergy-Pontoise, 5 mail Gay-Lussac, Cergy-Pontoise Cedex, 95031, France.

[2] École Polytechnique Fédérale de Lausanne, Institute of Chemical Science and Engineering (ISIC), CH-1015 Lausanne, Switzerland

[3] Department of Physics, Alzahra University, Tehran 1993893973, Iran

[4] Kaunas University of Technology, Department of Polymer Chemistry and Technology, Radvilenu pl. 19, LT-50254, Kaunas, Lithuania

Keywords: dft, energy disorder, interfaces, solar cells, perovskites, interaction energy

Abstract

Two spiro-MeTAD compounds (**1** and **2**) were synthesized, characterized by experimental and quantum mechanical methods, and used as hole transporting materials (HTMs) in perovskite solar cells (PSC). The new compounds differ from spiro-OMeTAD only by the presence of methyl substituents as compared to methoxy groups. This modification results in absorption-band blue shift by ~20 nm as compared to spiro-OMeTAD, increased glass transition temperature for 2, and reduced ionization potentials by 0.02-0.12 eV. Compared to the time-of-flight hole mobility of 9.10^{-4} cm^2/Vs measured for spiro-OMeTAD in vacuum-deposited layers, hole mobilities larger by five times were obtained for spiro-MeTAD compounds, ranging between $2\text{-}5.10^{-3}$ cm^2/Vs. Despite this improvement, J-V measurements in PSCs resulted in power conversion efficiency (PCE) of 17.2% and 17.05% for **1** and **2** HTMs, respectively, as compared to 19.24 % for spiro-OMeTAD. These results point to the dominant importance of the perovskite/HTM interfacial properties as compared to HTM hole-transport properties in the bulk. The impact of additives on the hole mobility of HTMs and on the PCEs is also discussed. Given that improved hole-mobility and energy-level alignment are the main targets of the current research efforts in this domain, our results alert on the necessity to give priority to improving perovskite-HTM interaction properties.

1. INTRODUCTION

Efficient and low cost solar-energy harvesting by means of photovoltaic devices constitutes one of the main objectives for present research. Among different solar cell concepts, dye sensitized solar cells (DSSC) and perovskite based solar cells (PSC) have shown increasing power conversion efficiencies (PCE) recently reaching 14.3%[1] and 25.2%[2], respectively. In both types of solar cells, the prevalently used hole transporting material (HTM) is 2,2′,7,7′-tetrakis(*N*,*N*-di-p-methoxyphenylamine)-9,9′-spirobifluorene (spiro-OMeTAD). While several phenomena jointly determine the solar cell performances, here we focus on the impact of the HTM properties in PSC.

The success of spiro-OMeTAD is supposed to reside at least on the good energy level matching between HOMO of this HTM with that of several dyes and of the perovskite absorber. However, this semiconductor suffers from low hole mobility of roughly 10^{-6}-10^{-5} cm^2/Vs in the amorphous phase,[3] reaching only ~10^{-3} cm^2/Vs in single crystals,[4] which constitutes an important drawback for its use in high efficiency photovoltaic devices. This issue has motivated intensive research efforts in order to replace spiro-OMeTAD by more efficient HTMs, which dominance has indeed been already overcome.[5-7] However, a general mechanism that could explain this success has not been identified so far, due to multiple differences between the new molecules and spiro-OMeTAD. Consequently, a seemingly random optimization process is still required with every new HTM, rendering their further development unpredictable, cost intensive, and inefficient.

As a means to render more efficient the research for new HTMs, a detailed analysis of the pros and cons of spiro-OMeTAD properties is needed. While detailed analyses on the hole mobility of amorphous spiro-OMeTAD are missing, interesting insights come from two recent studies: (i) a theoretical upper-limit hole mobility of roughly 4.10^{-3} cm^2/Vs was found along one crystallographic direction in spiro-OMeTAD single crystals,[4] which is due to large electronic couplings along this

direction, whereas vanishingly small electronic couplings as low as only a few meV were found along the other directions. Geometrical deformations, strong dipole moments, and steric hindrance were found to constitute the bottlenecks preventing spiro-OMeTAD from high hole mobility. Accordingly, very small electronic couplings and hole mobilities can be expected with regard to the hole mobility of spiro-OMeTAD in the amorphous phase. (ii) Important energy disorder in hole transport levels was found in amorphous spiro-OMeTAD, which, in the frame of a Gaussian distribution, was characterized by a standard deviation (σ-parameter) of 0.16 eV.[8]

The origin of the important σ value of spiro-OMeTAD can in part stem from the distribution of dipole moments ranging between 0-5.3 Debye[4] generated by the presence and random orientations of eight methoxy groups. Indeed, methoxy substituents in triphenylamine compounds were found to reduce the hole mobility as compared to the non-substituted one, due to the enhancement of the dipole moment and their disorder.[9-13] On the other hand, several methoxy- and methyl substituted triphenylamine-based compounds were found to transport holes faster than non-substituted ones in spite of important dipole moments,[14, 15] with better effect in the case of methyl substituents.[16] Detailed analysis of these contradictory results pointed to the competition between two factors playing important roles for the hole mobility:[16] (i) the permanent molecular dipole moments impacting negatively the hole transport, and (ii) the strength of intermolecular interaction. The latter factor was found to strongly reduce the intra- and intermolecular geometrical randomness and their contribution on the energy disorder.[16] Interestingly, it was found that the methyl substituents are able to enhance the intermolecular interactions, hence to reduce the geometrical disorder, without modifying the permanent dipole moments of the parent molecules. On the contrary, while the methoxy groups enhance the intermolecular interactions more importantly as compared to methyl groups, they increase the dipole moments of the parent molecules, thus destroying part of the beneficial effect stemming from the stronger intermolecular interactions.

Motivated by these results, and aiming to obtain new HTMs exhibiting improved hole transport properties, but very similar structural, electrochemical, and optical properties as compared to spiro-OMeTAD, here we present two new molecules called spiro-MeTAD-**1** and spiro-MeTAD-**2**, reported hereafter as **1** and **2**, differing from spiro-OMeTAD by only replacing the methoxy groups with methyl groups linked in different positions and different numbers. The basic idea was to reduce the energy disorder (value of σ-parameter) by removing the detrimental effect of the dipole moments induced by the methoxy groups. We show that the new compounds indeed exhibit smaller σ, higher hole mobility by at least five times as compared to spiro-OMeTAD, while simultaneously preserving similar electronic and structural characteristics as the original molecule. Interestingly, the use of these new compounds in the device structure of FTO/compactTiO_2/meso-porousTiO_2/perovskite/HTM/Au results in PCE of 17.2% and 17.05% for **1** and **2**-based devices, respectively, as compared to 19.2% for spiro-OMeTAD. In view of the better transport properties found for the new HTM compounds as compared to spiro-OMeTAD, the slightly smaller PCEs of the new HTMs point to the dominant importance of the perovskite/HTM interfacial properties.

In spite of the slightly smaller PCE of the new HTMs as compared to spiro-OMeTAD, their use in PS solar cells seems very promising. Last but not least, the new compounds are less costly than spiro-OMeTAD with respect to laboratory procedure, which may result in decreased cost efficiency of their use in PV devices.

The paper is organized as follows: we firstly focus on the intrinsic and bulk properties of the new compounds, after which we compare their performances in perovskite solar cells with respect to spiro-OMeTAD.

2. EXPERIMENTAL SECTION

2.1. **Materials.** *Synthesis*. 1-iodo-3,5-dimethylbenzene (98%), Copper iodide CuI (>99%), potassium phosphate K_3PO_4 (97%), lithium amide $LiNH_2$ (95%) were purchased from Alfa Aesar.

Sodium *tert*-butoxide (97%), palladium acetate $Pd(OAc)_2$ (98%), tri-*tert*-butylphosphine $P(tBu)_3$ (98%) were purchased from Aldrich. 2,2',7,7'-tetrabromo-9,9'-spirobifluorene (>98%) and *p,p'*-ditolylamine (>97%) were purchased from TCI Chemicals. DMF and toluene were dried by distillation from calcium hydride CaH_2 and sodium metal, respectively. Column chromatography and TLC were performed on silica gel 60 (230-400 mesh, Merck) and silica gel 60 F254 plates (Merck), respectively.

Devices. PbI_2 and $PbBr_2$ were purchased from TCI Chemicals. Cesium iodide CsI was purchased from abcr GmbH. FAI was purchased from Dyesol. Anhydrous DMF and DMSO were purchased from Acros Chemicals.

2.2. Characterizations. ^1H and ^{13}C NMR spectra were recorded on a Bruker DPX-400 NMR spectrometer in 5 mm tubes with $CDCl_3$ as solvent in all cases. The ^1H and ^{13}C chemical shifts were referenced to solvent peaks, 7.26 and 77.2 ppm, respectively. High-resolution mass spectroscopy was performed by the CNRS IMAGIF in Gif-sur-Yvette. Thermogravimetric analysis (TGA) was carried out on a TA Instrument Q50 TGA under argon flow at a heating rate of 20°C/min. The temperature of thermal degradation ($T_d^{5\%}$) was measured at the point of 5% weight loss. Differential scanning calorimetry analysis (DSC) was performed on a TA Instruments Q100 calorimeter, calibrated with indium and flushed with argon. Samples were scanned from 0 °C to 200 °C at a heating rate of 20°C/min then rapidly cooled to 0 °C (quenching) and heated at the same rate to 200 °C. UV-Vis measurements were performed at room temperature in spectrometric-grade THF solutions and on glass subtrates using a Jasco (V-570) spectrometer. Cyclic voltamperometry (CV) was carried out using an Autolab (AU128N, FRA2) electrochemical analyser with Pt disc used as working and counter electrodes and Ag wire as pseudo-reference. The three electrodes were immersed in a CH_2Cl_2 solution with 0.1 M tetrabutylammonium hexafluorophosphate (n-Bu_4PF_6)

and 10^{-3} M **1** or **2** derivatives. Ferrocenium/ferrocene (Fc^+/Fc) redox potential was measured in order to calibrate the pseudo-reference electrode.

2.3. Ionization potentials and hole mobility measurements. To obtain ionization potentials (IP^{PES}) of the compounds in solid-state, photoelectron emission spectra were taken under similar setup of electron photoemission spectrometry in air (PESA) as it was described elsewhere.[17] The vacuum-deposited films onto fluorine doped tin oxide glass substrates were fabricated for PESA measurements. The samples under electric field of 10^3 V/cm were excited by monochromatic light of different photon energies utilizing coupled monochromator (CM110 1/8m) and deep UV deuterium lamp ASBN-D130-CM. Electron photoemission current at a counter electrode under different excitations were measured by the 6517B Keithley electrometer. IP^{PES} values were taken from corresponding photoelectron emission spectra as it was described previously.[18]

To investigate hole-transporting properties of the compounds in diode-like indium tin oxide (ITO)/tested film/Al structures, two methods, i.e. time-of-flight (TOF) and photo charge carrier extraction by linearly increasing voltage (Photo-CELIV) were used. For the TOF measurements, 1.3-3.1 μm thick films were deposited by thermo-vacuum evaporation technique exploiting vacuum equipment from Kurt J. Lesker in-built in an MB EcoVap4G glove box. For the Photo-CELIV measurements, 0.4-0.6 μm thick films with and without additives were spin-coated utilizing the spin coater SPIN 150. The conditions of the preparation of the samples with additives was the same as it is described below for the preparation of devices. The Nd:YAG laser EKSPLA NL300 (355 nm, 3-6 ns) was used as the excitation source in setups of both TOF and Photo-CELIV. The corresponding current transients were recorded by oscilloscope Tektronix TDS 3032C. Different voltages were applied to the samples in the TOF experiments using the Keithley 6517B electrometer. Hole mobility at different electric fields was calculated by the formula $\mu_{TOF}=d^2/V \cdot t_{tr}$ having layer thickness *(d)*, applied voltage (*V)*, and transit time (t_{tr}) taken from the TOF transients. The triangle

pulse with pulse duration (t_{pulse}) of 10 μs and different amplitudes (U) was applied to the samples in the Photo-CELIV experiments using the functional generator Tektronix AFG3011C. Hole mobilities were calculated at different electric fields by the formula $\mu_{CELIV}=2d^2/A\cdot t_{max}^2$ having the slope $A=U/t_{pulse}$ of triangle pulse and time (t_{max}) taken at the moment when maximum was seen in the CELIV photocurrent transients.[19]

2.4. Synthesis of target molecules. *Synthesis of compound **4***. To a solution of 1-iodo-3,5-dimethylbenzene (2.1 g, 9 mmol) in dry DMF (25 mL) were added $LiNH_2$ (414 mg, 18 mmol), K_3PO_4 (1.91 g, 9 mmol) and CuI (171 mg, 0.9 mmol) under argon. The reaction mixture was heated at 130 °C for 24 h. After cooling, the solution was filtered under celite and the solid washed with CH_2Cl_2 (100 mL). The organic phase was washed with water (4×25 mL) and dried with $MgSO_4$. After evaporation of solvent, the residue was purified by column chromatography (SiO_2) with cyclohexane/ CH_2Cl_2 (1/1) as eluent to obtain white solid (740 mg, 75%). ^{1}H NMR ($CDCl_3$) δ 6.71 (s, 4H), 6.60 (s, 2H), 2.29 (s, 12H). ^{13}C NMR ($CDCl_3$) δ 143.2, 139.0, 122.8, 115.8, 21.43.

*General procedure for the synthesis of **1** and **2***. To a solution of 2,2',7,7'-tetrabromo-9,9'-spirobifluorene (0.5 mmol) in dry toluene (15 mL) were added diphenylamine **3** or **4** (2.5 mmol), sodium *tert*-butoxide (288 mg, 3 mmol) and $Pd(OAc)_2$ (6 mg, 0.025 mmol). The solution was degassed with argon for 30 min. Then P(*t*Bu)$_3$ (10 mg, 0,05 mmol) was added and the reaction mixture was refluxed (115 °C) for 12 h. After cooling, the solution was poured into 30 mL of water. The aqueous layer was extracted with ethyl acetate (2×30 mL).The organic phase was washed with brine (3×20 mL) and water (2×20 mL) and dried with $MgSO_4$. After evaporation of solvent, the residue was purified by column chromatography (SiO_2) with cyclohexane/ CH_2Cl_2 (7/3) as eluent.

1: white solid, 85% yield. ^{1}H NMR (400 MHz, $CDCl_3$): δ = 7.39 (d, J = 8.2 Hz, 4H), 7.15-7.02 (m, 18H), 7.02-6.82 (m, 18H), 6.69 (s, 4H), 2.32 (s, 24H, CH_3); ^{13}C NMR (101 MHz, $CDCl_3$):

δ= 150.2, 146.9, 136.3, 131.7, 129.7, 124.2, 123.4, 120.1, 119.5, 77.3, 20.8; HRMS (ESI+) calculated for M+: 1096.5438, found: 1096.5465.

2: white solid, 78% yield. ^{1}H NMR (400 MHz, $CDCl_3$): δ= 7.36 (d, J = 7.8 Hz, 4H), 7.08-6.95 (m, 4H), 6.93-6.72 (m, 28H), 2.28 (s, 48H, CH_3); ^{13}C NMR (101 MHz, $CDCl_3$): δ= 149.6, 147.5, 146.6, 138.6, 124.4, 123.2, 122.3, 122.0, 121.9, 119.9, 119.7, 118.6, 77.2, 21.6; HRMS (ESI+) calculated for M+: 1208.6713, found: 1208.6744.

2.5. Device fabrication. After rinsing with deionised water, acetone, and ethanol, the FTO coated-glass substrate were further cleaned with UV ozone treatment for 15 min. Then, 30 nm TiO_2 compact layer was deposited on FTO via spray pyrolysis using O_2 as carrier gas at 450 °C from a precursor solution of titanium diisopropoxide in anhydrous ethanol with the molarity of 0.2 M. Then, a mesoporous TiO_2 layer was deposited by spin coating for 15 s at 5000 rpm with a ramp of 2000 rpm/s, using a 30 nm particle paste (Dyesol) diluted in ethanol with weight ratio of 1:6. After the spin coating, the substrates were sintered at 450 °C for 30 min under dry air flow.

The perovskite composition used for this study is $Cs_{0.1}FA_{0.9}Pb(I_{0.9}Br_{0.1})_3$. The perovskite precursor solution was prepared by dissolving of FAI, PbI_2, CsI and $PbBr_2$ powder in anhydrous DMF:DMSO 4:1 (v:v) and the molarity of solution is fixed 1.35 M. This solution was kept at 70 °C for 30 min. The perovskite solution was spin coated in a two steps program at 2000 and 6000 rpm for 10 and 20 s, respectively. During the second step, 200 µL of chlorobenzene was poured on the spinning substrate 10 s prior to the end of the program. The substrates were then annealed (usually at 100 °C) for 1 h in a dry box. The substrates were cooled down for few minutes and a spiro-OMeTAD solution (74 mM in chlorobenzene) was spin coated at 4000 rpm for 20 s. Spiro-OMeTAD was doped with Li-TFSI salt and TBP. The molar ratio of additives for spiro-OMeTAD was: 0.5, and 3.3 for Li-TFSI, and TBP, respectively. For spiro-MeTAD labelled as **1** and **2**, the molarity of solution was chosen as 37 mM with the same molar ratio of additive. We also investigate the effect

of molar ratio of the additives. For spiro-MeTAD labelled as **1-2** and **2-2**, the molar ratio of additives was selected as: 1 and 6.6 for Li-TFSI, and TBP with the same solution molarity of 37 mM, respectively. Finally, 70-80 nm of gold top electrode was thermally evaporated under high vacuum.

A spectrophotometer (Varian Cary5) was used to measure UV–Vis absorption spectra of the samples. Current-voltage characteristics are measured by a digital source meter (Keithley 2400) with voltage scan rate of 10 mV/s using a 450 W xenon light source under AM 1.5G. IPCE spectra were measured under constant white light bias with an intensity of 10 mW/cm^2 through a Gemini-180 double monochromator.

2.6. Computational Details. Density functional methods (DFT)[20] by employing the B3LYP[21, 22] and ωB97X-D[23] functionals in conjunction with the 6-31G* basis set were used in this study. Symmetry unconstrained geometry optimizations were carried out on the isolated molecules and on four type of dimers constructed for each of compounds spiro-OMeTAD and 1 (Annex I, SI). Frequency calculations for the isolated molecules and for the dimers indicated in all cases presence of only positive frequencies, thus assuring that the obtained geometries correspond to minimum points on the potential surfaces of individual molecules or dimers. The intermolecular interaction energy calculations were performed with the ωB97X-D functional and the same basis set. The interaction energies calculated on the bases of the total energies of the isolated molecules and of th e dimers were subsequently corrected for the zero point energy (ZPE), and for the basis set superposition error (BSSE) following the counterpoise method. The B3LYP functional was used for the rest of the calculations. The optical properties of the monomers and dimers were calculated by means of the time dependent density functional theory method (TDDFT).[24-28] The vertical ionization potentials (IP) were calculated as energy difference between neutral and cation radical species at the neutral state geometry. The intramolecular reorganization energies (λ_i) were calculated in the frame of the potential surface method.[29] The electronic couplings between the

molecular orbitals were calculated according to the direct interaction method.[30] All calculations were performed with Gaussian 09 program.[31] A more detailed description on the choice of the theoretical method and the theoretical model compounds and dimers is given in Annex I in the Supporting Information (SI).

3. RESULTS AND DISCUSSION

3.1 Synthesis and thermal characteristics

The synthetic route for the studied compounds is outlined in **scheme 1**. *p,p'*-ditolylamine **3** is a commercially available product. Diphenylamine intermediate **4** was synthetized by a Cu-catalysed amination of 1-iodo-3,5-dimethylbenzene. Spiro derivatives **1** and **2** containing substituted methyl functional groups were synthesized by the Buchwald-Hartwig amination reaction, carried out between 2,2',7,7'-tetrabromo-9,9'-spirobifluorene and the respective bis(methylphenyl)amines containing *p*-Me or *m,m*-Me substituents (**3** or **4** respectively). The two spiro-MeTAD compounds were purified by column chromatography and characterized by NMR spectroscopy (^{1}H and ^{13}C) and mass spectrometry. All the analytical data were consistent with the proposed structures. The two compounds have a good solubility in all of the common organic solvents.

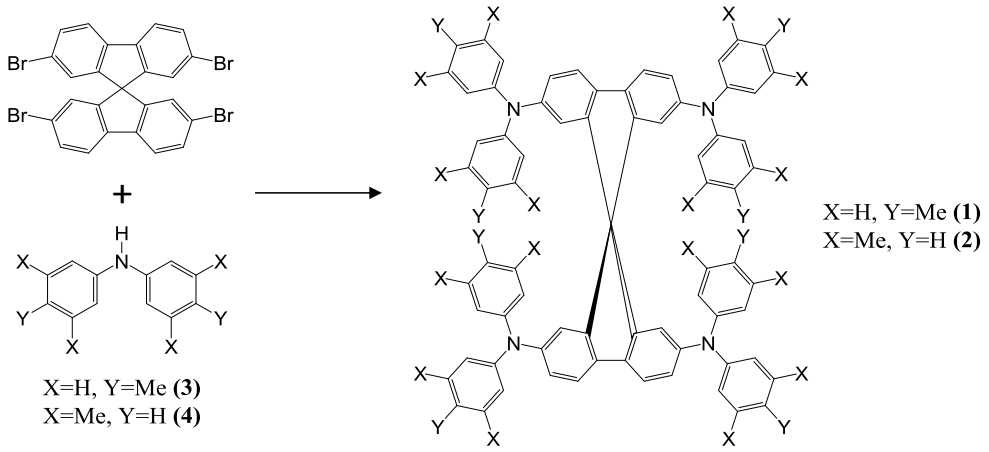

Scheme 1. Synthesis of compounds **1-2** (Reagents and conditions: sodium *tert*-butoxide, $Pd(OAc)_2$, $P(tBu)_3$, toluene, 115 °C, 12 h.)

It is worth noting that following the same synthesis path, the yields of compound **1** and **2** are roughly 20-30% larger as compared to that of spiro-OMeTAD. This is due to the smaller amount of solvent and shorter time needed for the separation of the new compounds by chromatographic methods as compared to spiro-OMeTAD. While we are not able to evaluate the impact of this aspect at the industrial level, we believe that the same trend might be observed in both laboratory- and industrial synthesis conditions.

Thermal properties of **1** and **2** were investigated by thermogravimetric analysis (TGA) and differential scanning calorimetry (DSC) under argon atmosphere. The thermal decomposition (T_d) and the glass transition (T_g) temperatures are summarized in **Table 1**. **1** and **2** showed high thermal stabilities with $T_d^{5\%}$ values superior to 400 °C, which are high enough for applications in optoelectronic devices. Confirmed by DSC analysis, compounds **1** and **2** are revealed as amorphous materials. All compounds exhibit high glass transition temperatures (T_g) ranging from 96 to 143 °C. In particular, compound **2** shows a significant increase in T_g (143 °C) compared to spiro-OMeTAD (110 °C), which may lead to better thermal stability of the device over time.

Table 1. The thermal characteristics of spiro-OMeTAD and compounds **1** and **2**.

Molecules	$T_d^{5\%}$ (°C)	T_g (°C)
1	450	96
2	443	143
spiro-OMeTAD	424	110

3.2 Characteristics of pristine compounds

3.2.1 Geometries and frontier orbitals of isolated compounds

The geometries of compounds **1** and **2** obtained in the absence of medium effects ("gas phase") are shown in **Figure 1a**. The geometry of spiro-OMeTAD is also shown for comparison. Except for the substitutions on the diphenylamine moieties, quite similar global geometries were obtained.

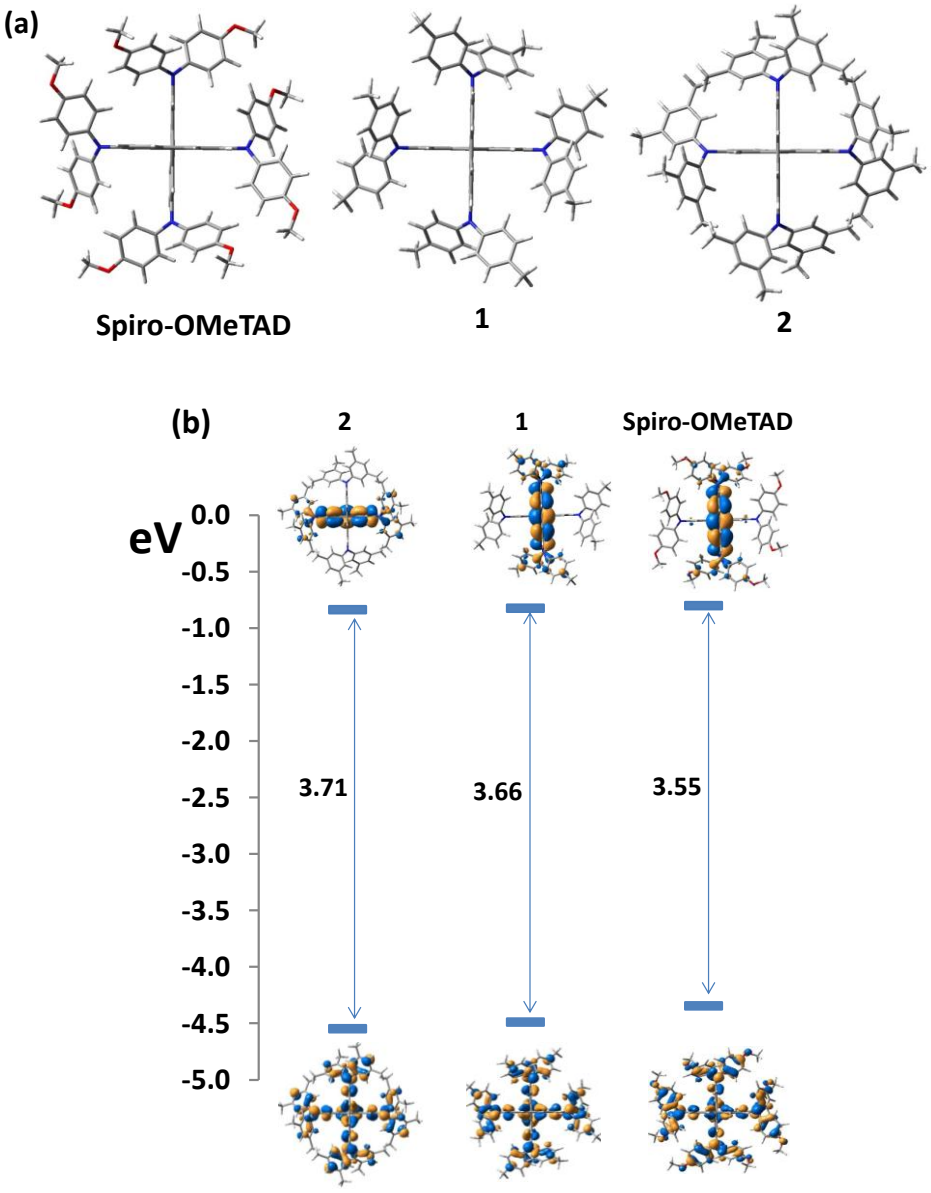

Figure 1. (a) Geometries of spiro-OMeTAD (with orientation of methoxy groups arbitrary chosen) and of compounds **1** and **2** obtained at the ωB97XD/6-31G* level ("gas phase"). (b) Energy diagram corresponding to frontier orbitals of spiro-OMeTAD and compounds **1** and **2** obtained at B3LYP/6-31G* level in gas phase. The HOMO and LUMO representations are also shown. The left-right ordering of the compounds follows the increasing HOMO energy.

The HOMOs and LUMOs of spiro-OMeTAD and compounds **1** and **2** also show quite similar shapes, with the dominant contribution coming from the spirofluorene moieties (**Figure 2**). Both HOMO and LUMO levels of spiro-OMeTAD are higher than those of compounds **1** and **2** (**Table 2**), which is due to the π-donor effect of the methoxy groups in the former case. Nevertheless, this effect is more pronounced in the case of HOMOs due to their important delocalization over the peripheral di-phenyl moieties, thus resulting in smaller HOMO-LUMO gap in the case of spiro-OMeTAD as compared to compounds **1** and **2**. It is worth noting that the delocalization of the HOMOs over both fluorene moieties (**Figure 2**) is expected to be strongly affected by the geometrical deformations occurring in the real materials,[4] in which case HOMO localization on only one of the arms is to be expected.

3.2.2 Impact of substituents on the strength of intermolecular interactions

The replacement of methoxy groups of spiro-OMeTAD by one or more methyl groups is expected to influence the strength of intermolecular interactions in the bulk of these materials. Indeed, changes in the intra- and intermolecular geometrical randomness, directly impacting the energy disorder and hole mobility, have already been reported.[16] Additionally and importantly, the methyl *vs* methoxy substituents are expected to impact on the perovskite-HTM interfacial interactions.

In order to obtain some insight on these aspects, four model dimers were optimized for spiro-OMeTAD and compound **1** (**Figure 2**). The average dissociation energy in the case of **1** is larger than for spiro-OMeTAD (23 kcal/mol and 12 kcal/mol respectively) indicating that *the intermolecular interactions are strengthened upon methyl substitutions*. In the following we show that the stronger intermolecular interactions for compounds **1** and **2** as compared to spiro-OMeTAD impact several properties, such as polarization energies in the

bulk of these materials, hole transport properties, and characteristics of layer-deposition from solutions.

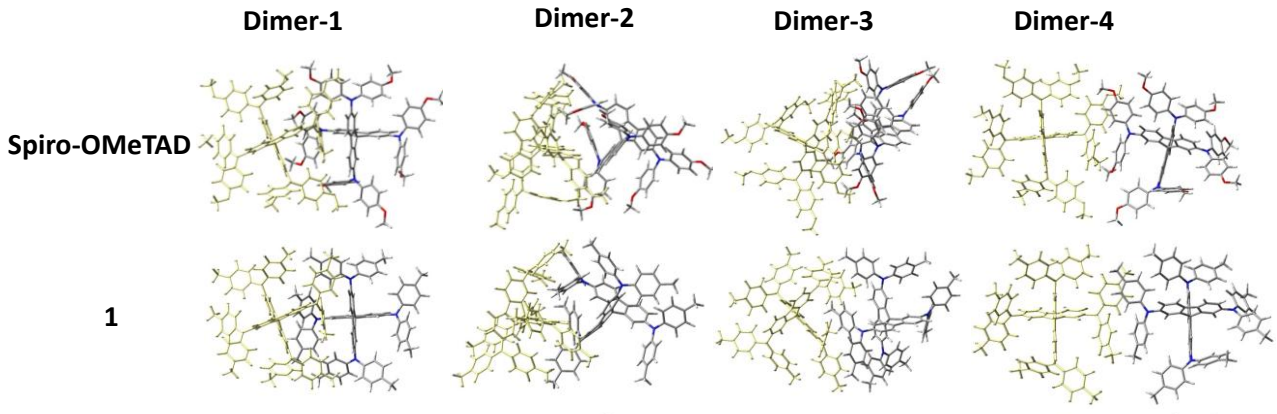

Figure 2. Geometries of four dimer types constructed with spiro-OMeTAD and compound **1**, obtained at the ωB97XD/6-31G* level ("gas phase"). For clearer representation, one molecule of each dimer is highlighted in yellow. Note that in each dimer type, the intermolecular interactions in the case of spiro-OMeTAD and of compound **1** involve strictly equivalent molecular moieties, which allows for a pertinent comparison between the corresponding dissociation energies.

3.2.3 Physical and optical properties

Cyclic voltammetry (CV) was employed to investigate the redox properties and to estimate the ionization potentials (IP^{SS}) of compounds. The ionization potentials were additionally determined by photoelectron spectroscopy in air (IP^{PES}). The results of these measurements on compounds **1** and **2** and spiro-OMeTAD are shown in **Figure 3** and in **Table 2**.

Table 2. Ionization potentials (IP^{SS}) (and electron affinities (EA^{SS})) from cyclic voltammetry (and optical band gap E_g^{opt}), ionization potentials from photoelectron emission spectra (IP^{PES}), and HOMO (ε_{HOMO}) and LUMO (ε_{LUMO}) energies (B3LYP/6-31G* level in "gas" phase) corresponding to compounds **1, 2** and Spiro-OMeTAD.

Compound	E_{ox} vs Fc/Fc^+ (V)	IP^{SS} (eV)	EA^{SS} (eV)	IP^{PES} (eV)	ε_{HOMO} (eV)	ε_{LUMO} (eV)
spiro-OMeTAD	0.04	4.84	1.84	4.94	-4.35	-0.80
1	0.08	4.88	1.82	4.92	-4.49	-0.83
2	0.055	4.86	1.80	4.90	-4.55	-0.84

IP^{SS} and EA^{SS} values were estimated by using the ferrocene (Fc) ionization potential value (4.8 eV) as external standard, according to the following equations: $E_g^{opt} = 1240/\lambda_{onset}$, $I_p^{SS} = 4.8+E_{1/2}^{vs\ Fc}$, $E_A^{SS} = I_p^{SS} - E_g^{opt}$. E_g^{opt} designs the optical band gaps estimated from the edges of electronic absorption spectra.

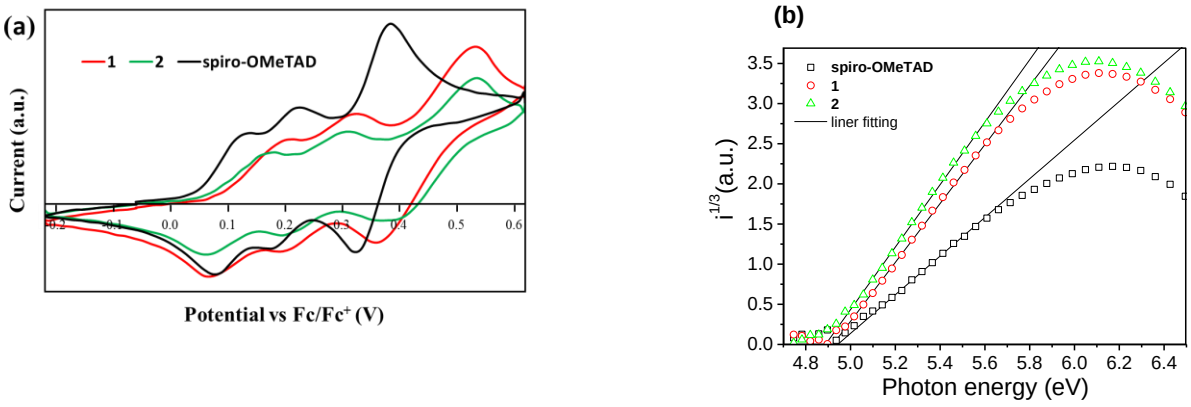

Figure 3. (a) Cyclic voltammograms (CV) of compounds **1**, **2** and spiro-OMeTAD in 10^{-3} M CH_2Cl_2 solutions at sweep rate of 100 mV/s, 0.1 M *n*-Bu_4PF_6. **(b)** Photoelectron emission spectra of the film for vacuum deposited compounds.

Both IP^{SS} and IP^{PES} datasets provide similar trends between the spiro-MeTAD compounds, with **1** < **2**. Interestingly, the two experimental methods indicate opposite trends between spiro-OMeTAD and spiro-MeTAD IP values: IP^{SS} value of spiro-OMeTAD (4.84 eV) is smaller- whereas IP^{PES} value (4.94 eV) is larger as compared to spiro-MeTAD ones. The theoretical $-\varepsilon_{HOMO}$ values

(representing the ionization energies deduced in the frame of Koopmans' theorem) are in better agreement with the IP^{SS} values, although an inversion can be observed in the latter values between compounds **1** and **2**. These discrepancies point to the crucial role of the polarization energy in different media, which are expected to vary significantly between the isolated compounds (absence of contributions from the polarization energy during theoretical calculations), the solution state with presence of electric field around the electrode in CV, and the condensed packed solid films obtained by vacuum evaporation (PES measurements). The decreasing IP^{PES} in the order spiro-OMeTAD > **1** > **2** might correlate with the increasing intramolecular interaction energies in the same order, in turn enhancing the intermolecular polarization energy in the vacuum deposited layers. It is worth mentioning that both IP^{SS} and IP^{PES} values for vacuum deposited pristine spiro-OMeTAD without additives (4.84 eV and 4.94 eV respectively) are smaller than the reported value of 5.1 eV for solution prepared Spiro-OMeTAD with LiTFSI and TBP, again indicating the strong dependence of this parameter on the environment conditions and additives type.[32]

Despite the above discrepancies, the two experimental datasets indicate global variation by only 0.04 eV, accordingly suggesting small variation on the V_{oc} values in solar cell applications.

Optical properties of compounds **1** and **2** were examined in dilute THF solution and in the thin film solid state. The experimental absorption spectra are shown in **Figure 4**, whereas the λ_{max} wavelengths are collected in **Table 3**. All compounds exhibit similar optical behaviour in dilute solution, with a strong absorption band located in the UV spectral domain (380-400 nm). It should be noted that the absorption peaks of the two compounds 1 and 2, both in solution and in the solid state, are narrower than those of spiro-OMeTAD allowing a better transparency of the HTM layer. The optical band gaps (E_g^{opt}) of **1-2** and spiro-OMeTAD were estimated from the edge of the first absorption peak in solution (**Table 3**). The smaller bandgap of spiro-OMeTAD as compared to compounds **1** and **2** seems to correlate with the similar trend of the corresponding HOMO-LUMO gaps (see **Figure 1**).

Photoluminescence spectra of HTMs in chlorobenzene are shown in **Figure 4c**. The trend of the emission peaks at 420 nm for spiro-OMeTAD[33, 34] and at 407 nm for compounds **1** and **2** is in line with the similar trend of the absorption onset wavelengths and with the one between the corresponding HOMO-LUMO gaps.

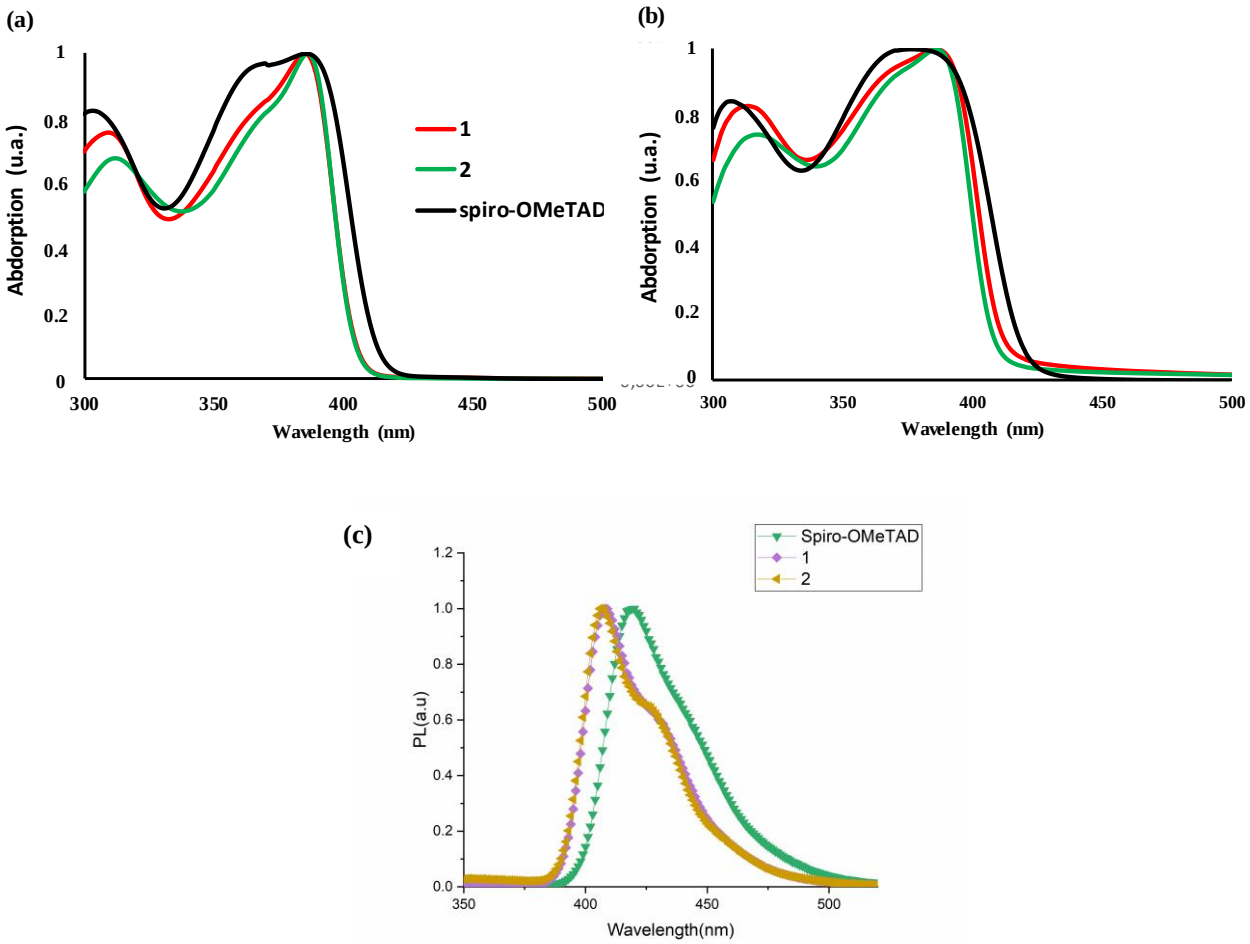

Figure 4. UV spectra of **(a)** dilute THF solutions (normalized at Abs = 1), and **(b)** in solid state (spin coated on glass) of compounds **1**, **2** and spiro-OMeTAD. **(c)** Photoluminescence spectra of **1**, **2** and spiro-OMeTAD ($1 \cdot 10^{-5}$ M) in chlorobenzene.

Table 3. Optical characteristics of compounds **1**, **2** and spiro-OMeTAD. The values in parentheses correspond to the theoretical values (B3LYP/6-31G* level in gas phase). The two theoretical values

in the case of spiro-OMeTAD correspond to two different combinations between O-CH_3 bond orientations.

Compound	λ_{max} (solution, nm)	λ_{onset} (solution, nm)	λ_{max} (solid, nm)	E_g^{opt} (eV)
1	385 (389)	404	386	3.06
2	386 (386)	404	386	3.06
spiro-OMeTAD	386 (393-404)	412	378	3.0

3.2.4 Charge transport properties

Figure 5 shows electric field dependence of hole-drift mobility of compounds **1**, **2** and spiro-OMeTAD at room temperature (RT), measured by the time-of-flight (TOF) method in vacuum deposited layers, and by the CELIV method in spin-coated layers with and without additives (Experimental section).

TOF hole mobilities. Hole mobilities of roughly five times faster (*ca.* $5 \cdot 10^{-3}$ cm^2/Vs) were recorded at an electric field of $3.6 \cdot 10^5$ V/cm for the layers of compounds **1** and **2**, as compared to spiro-OMeTAD ($9 \cdot 10^{-4}$ cm^2/Vs). Moreover, current-time signals shown in **Figure S1** (Supporting information, SI) suggest less dispersive hole transport for compounds **1** and **2**, which comforts the conclusion that the new compounds globally exhibit improved hole-transport properties as compared to spiro-OMeTAD.

It is worth noting that the hole mobility found for the vacuum-evaporated "home-made" spiro-OMeTAD is at least 1-2 orders of magnitude larger than values found in literature for spin coated layers ($4 \cdot 10^{-5}$ cm^2/Vs and $1.7 \cdot 10^{-6}$ cm^2/Vs from SCLC[3] and FET[35] measurements, respectively) and

only one order of magnitude smaller than the FET value of $1.3 \cdot 10^{-3}$ cm^2/Vs found for single crystals of spiro-OMeTAD.[35] While these comparisons suggest enhanced degree of ordering in our layers obtained by vacuum evaporation, the pertinent information remains that the transport properties of the methyl-containing compounds **1** and **2** are improved as compared to spiro-OMeTAD.

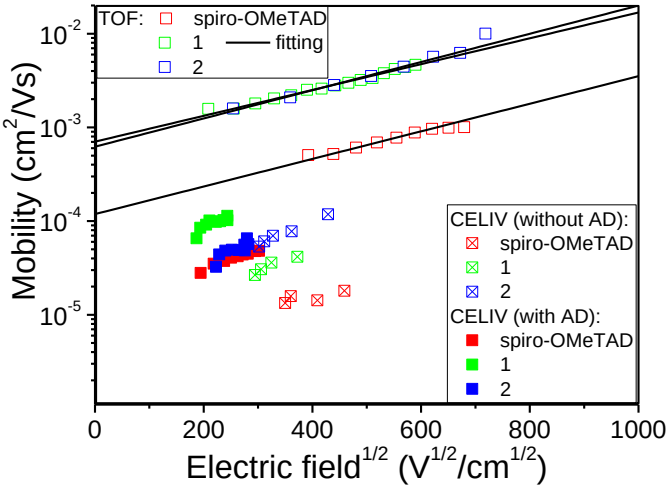

Figure 5. Electric field dependencies of hole-drift mobility of compounds **1**, **2** and spiro-OMeTAD in vacuum deposited layers (measured by the TOF method) and spin-coated layers with and without additives (AD) (measured by the CELIV method) at room temperature (RT).

Table 4. Hole transport parameters of compounds **1**, **2** and spiro-OMeTAD. The hole mobilities are approximate values taken at the electric field of $3.6 \cdot 10^4$ V/cm. Theoretical parameters calculated for compounds **1**, **2** and spiro-OMeTAD at the B3LYP/6-31G* and ωB97WD/6-31G* levels in gas phase are also given, such as HOMO and LUMO energies, intramolecular reorganization energies (λ_h), HOMO-HOMO electronic couplings ($t_{H\text{-}H}$) deduced from a selected set of optimized dimers (average over 4 dimers for each compound, **Figure 2**), and dipole moments of isolated compounds.

Compound	μ	σ	μ_0	λ_h	$t_{H\text{-}H}$	Dip. Mom.

	(cm^2/Vs)	(eV)	(cm^2/Vs)	(eV)	(eV)	(Debye)
1	$5 \cdot 10^{-3}$	0.084	0.090	0.213	0.003	0.001
2	$5 \cdot 10^{-3}$	0.086	0.104	0.375	-	0.05
spiro-OMeTAD	$9 \cdot 10^{-4}$	0.106	0.360	0.133	0.004	0 - 5.3*

*****range of dipole moments obtained by considering a "random" orientation of the methoxy groups (selection of relative orientations).

In order to obtain some insight on the reasons for the observed improvements, temperature dependent TOF hole-mobility measurements were performed, and different intra- and intermolecular properties for compounds **1**, **2** and spiro-OMeTAD were calculated. Additionally, four model dimers were optimized for each compound (**Figure 2**) and the HOMO-HOMO electronic couplings between adjacent molecules were calculated.

The energetic disorder parameter (σ, **Table 4**) was deduced within the Gaussian disorder model, according to the following equation:[36]

$$\mu = \mu_0 \exp[-(\frac{2\hat{\sigma}}{3})^2] \exp[C(\hat{\sigma}^2 - \Sigma^2)E^{1/2}] \quad (1)$$

Here, σ is the standard deviation of the hopping site manifold, Σ is the positional disorder, C is a constant, and $\hat{\sigma} = \sigma/kT$.

Details on different methods are given in the **Figures S2, S3, and S4** (SI) and only selected numerical results are given in **Table 4**. The important result is that the energetic disorder parameter σ decreases importantly from 0.106 eV to 0.084 eV in the order spiro-OMeTAD > **2** = **1** (**Table 4**), which is consistent with the increasing hole-mobilities in the same order. Interestingly, the largest μ_0 value, which characterizes the intramolecular charge transport properties, was obtained for spiro-OMeTAD (0.36 cm^2/Vs, **Table 4**). Given the similar electronic couplings shown in **Table 4**, the larger μ_0 of spiro-OMeTAD simply translates to

lower intramolecular reorganization energies λ_h as compared to **1** and **2** compounds. However, the highest σ and the lowest mobility values found for spiro-OMeTAD suggest that the differences in the hole mobilities of these compounds are dominated by disorder phenomena. Indeed, the almost zero dipole moments of the methylated compounds (**Table 4**) indicate absence of the detrimental effect from the dipole-moment disorder. This effect is in strike contrast to the large dipole moments as high as 5.3 Debye calculated for spiro-OMeTAD, which has been found to negatively impact the charge-transport properties of organic semiconductors.[9-12] Additionally, stronger intermolecular interactions were calculated for the **1** compound as compared to spiro-OMeTAD (**Table 4**), which effect has been shown to reduce the geometrical contribution to the disorder parameter of **1** and **2** compounds as compared to methoxy-substituted ones.[16]

The global hole mobility improvement for methyl-substituted compounds *wrt* spiro-OMeTAD results consequently from a delicate balance between two opposite factors, the positive effect being dominant: (i) detrimental increase in intramolecular reorganization energy (λ_h), and (ii) positive impact from the decrease in energy disorder parameter (σ), in turn stemming from the decrease in dipole moment.

CELIV hole mobilities. The electric field dependences of CELIV hole mobilities in spin-coated layers of pure spiro-OMeTAD and spiro-MeTAD compounds are shown in **Figure 5**. Similar global trends *wrt* TOF results can be observed, with hole mobilities increasing in the order spiro-OMeTAD < **1** < **2**.

In view of the large utilization of additives in perovskite solar cells, we performed hole mobility measurements of spiro-OMeTAD, **1**, and **2** compounds in spin-cast layers with- and without additives. The results shown in **Figure 5** indicate hole-mobility improvement for spiro-OMeTAD and **1** compounds, but missing impact in the hole mobility of **2**. While the results for spiro-OMeTAD and **1** compounds correspond to the common-knowledge based expectations, the missing

sensitivity of **2** hole-mobility *wrt* the presence of additives is intriguing. We suspect these differences to correlate with the increasing intermolecular interaction energies, probably making the HTM-additives mixture less homogeneous in the case of strong HTM-HTM interactions.

3.3 Device characteristics

A schematic energy level diagram of the solar cell device is illustrated in **Figure 6**. After light absorption by the perovskite layer, photogenerated electrons and holes are moved to the photoanode (TiO_2 layer) and hole conductor layer, respectively. The HOMO level of HTMs should be higher than the valence band of the perovskite layer for hole extraction. As shown in CV results, the HOMO levels of both spiro-MeTAD compounds **1** and **2** are a little deeper than spiro-OMeTAD.

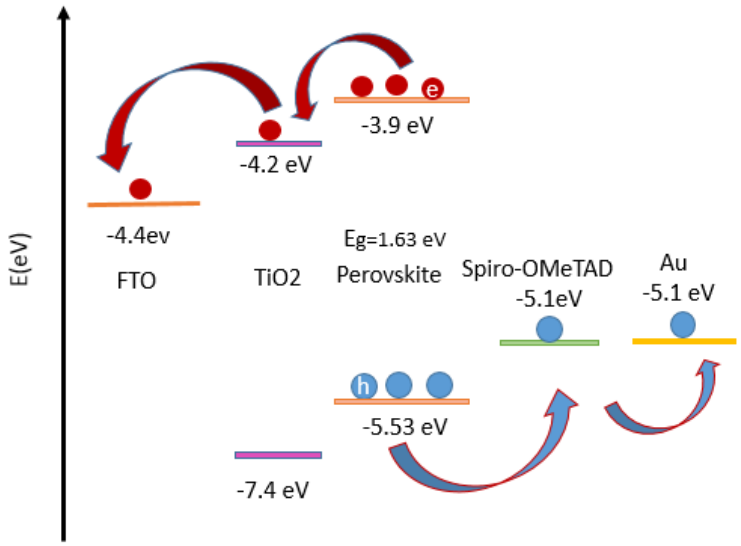

Figure 6. Schematic energy level diagram of the solar cell device. The ionization potentials of spiro-OMeTAD is as reported in Ref[32]

As shown in figure S7, the Scanning electron microscopy (SEM) images in cross-section view reveal that roughly 126-148 nm thick HTL has covered the perovskite film in devices based on new compounds while the thickness of spiro-OMeTAD is roughly 190-196 nm in control devices.

According to owing larger hole mobility, this thickness is appropriate for hole extraction process in new compounds-based devices, as proven in J-V characteristics.

Figure 7 shows photoluminescence spectra of perovskite-HTM systems for different HTMs deposited on the perovskite layer. The spectra show a band-edge transition of 773 nm related to the perovskite layer. The band-intensity corresponding to spiro-OMeTAD sample is lower than for other HTMs, indicating lower hole recombination or rapid extraction of holes across the interface.[37]

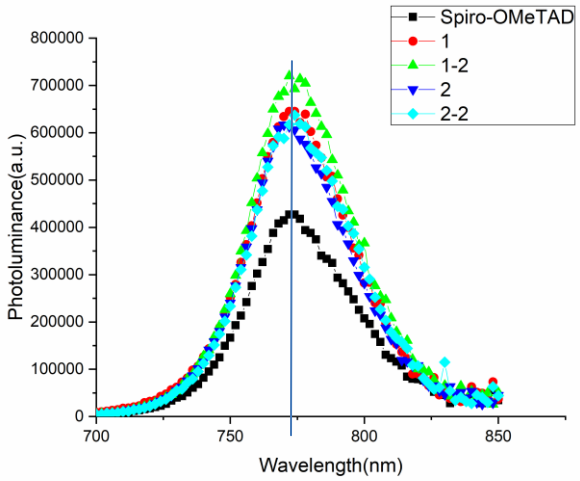

Figure 7. The PL spectra of the samples. The notations **1** and **1-2** correspond to two different concentrations of additives, with the concentration in the case of **1-2** being twice as large as the one for **1**. Same differences apply in the case of **2** and **2-2**.

Current-voltage characteristic curves are shown in **Figure 8** under sun illumination and in dark. The data is summarized in **Table 5**. The control sample with spiro-OMeTAD as HTM showed a power conversion efficiency (PCE) of 19.2% and 16.9% in backward and forward scan direction, respectively, with an open circuit voltage (V_{OC}) of 1.128 V, a short current density (J_{SC}) of 22.86 mA cm^{-2} and a fill factor (FF) of 74.6% under reverse scan conditions. For **1**-based devices we observe a small hysteresis with V_{OC} of 1.109 V, J_{SC} of 22.57 mA/cm^2, FF of 68.7% resulting in a PCE of 17.2% in backward scan. Spiro-OMeTAD-, 1-, and 2-based devices show hysteresis which can be due to inappropriate ambient atmospheric condition during the film deposition. Although the

highest PCE of 18.0% in backward voltage scan can be obtained for devices labelled as **2-2** with V_{OC} of 1.124 V, J_{SC} of 22.86 mA/cm^2 and FF of 70.2%, the hysteresis effect is increased as well with increasing concentration of additives (molar ratios of additives in **2-2** being two times larger as compared to **2**). Increasing the amount of additives has thus a negative impact on the photovoltaic performance of **1-2** and **2-2** -based devices. As shown, hysteresis is increased while PCE is decreased compared to **1** and **2** -based devices. Interestingly, the performances of spiro-OMeTAD PSCs remain basically unaffected when the additive amounts are increased by the same amount (two times).

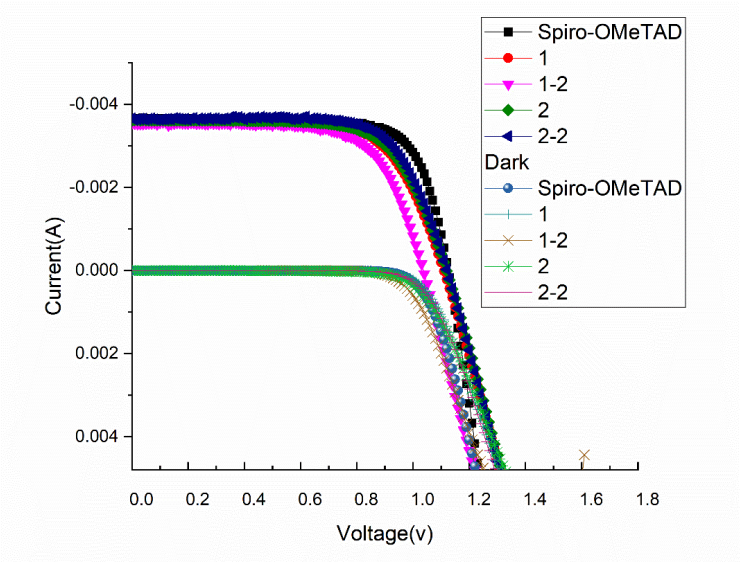

Figure 8. J-V curves of the best cells recorded with reverse (from V_{OC} to J_{SC}) scan direction.

Table 5. Photovoltaic parameters of different HTM based-devices under backward and forward scan direction.

HTM	Scan direction	J_{SC} (mA/cm^2)	V_{OC} (V)	PCE (%)	FF (%)	Integrated Jsc (IPCE)
Spiro-OMETAD	Rev	22.86	1.128	19.24	74.6	22.04
	For	23.19	1.085	16.99	67.5	

1	Rev	22.57	1.109	17.2	68.7	21.87
	For	21.29	1.099	15.38	65.7	
1-2	Rev	22.18	1.042	15.72	68	19.02
	For	22.45	0.984	10.28	46.5	
2	Rev	22.42	1.119	17.05	68	21.66
	For	22.91	1.086	15.24	62.1	
2-2	Rev	22.86	1.124	18.04	70.2	20.54
	For	23.28	1.074	12.18	48.7	

Photovoltaic parameters from different devices in backward direction are shown in **Figure 9**. **1**-based devices shows higher J_{SC} and lower Voc compared to **2**-based devices. **2**-based devices have the lowest fill factor, that we suspect is resulting from the inhomogeneity of film and interface problems. The average PCEs of **1**-based devices were 17% and the PCEs for **2**-based devices were 15%. With increasing additive concentration, **2-2** based devices show better performance in J_{SC}, V_{OC}, FF and PCE than **2**. These results revealed that the performance of **1** based device outperforms **2**.

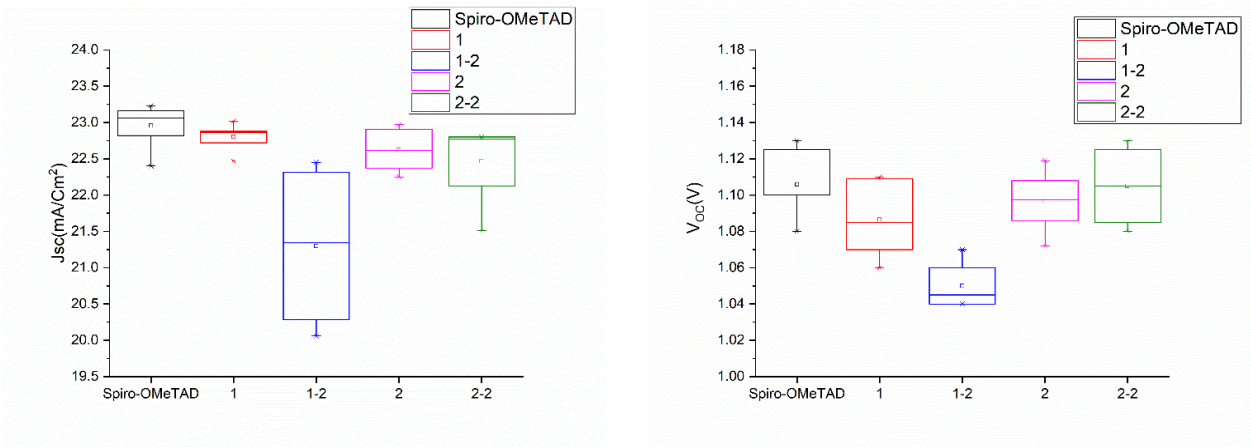

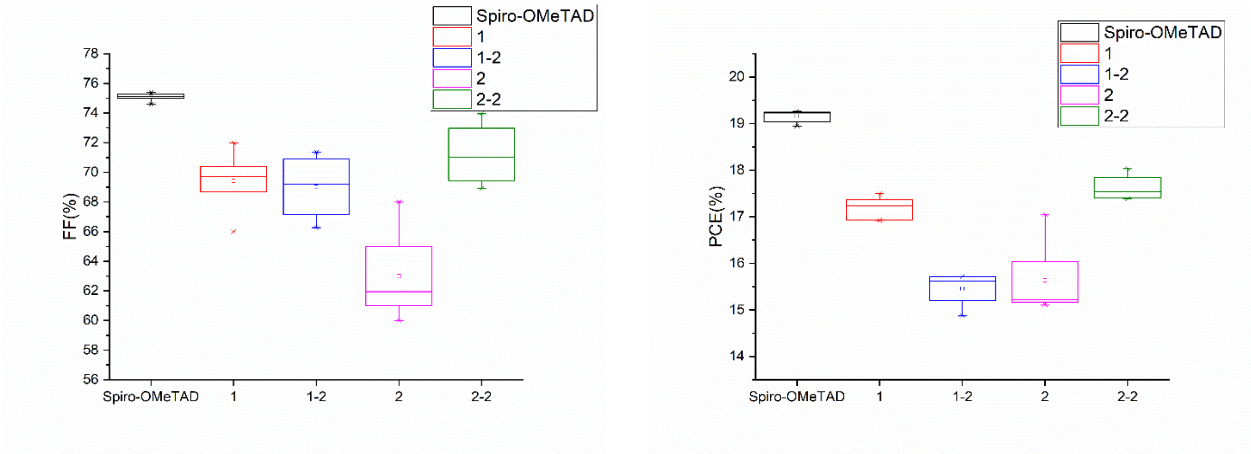

Figure 9. Statistical plot of J_{SC}, V_{OC}, FF and PCE of different devices.

Incident photon-to-current efficiency (IPCE) curves for devices are shown in **Figure 10**. The integrated current obtained by IPCE is 22.04, 21.87, 19.02, 21.66, and 20.54 mA/cm^2 for spiro-OMeTAD, **1**, **1-2**, **2** and **2-2** based devices, respectively. As shown in this figure, and from the integrated current obtained from IPCE, the obtained current decreased dramatically with increasing amount of additives. Intriguingly, this effect is less pronounced for **2** as compared **1**.

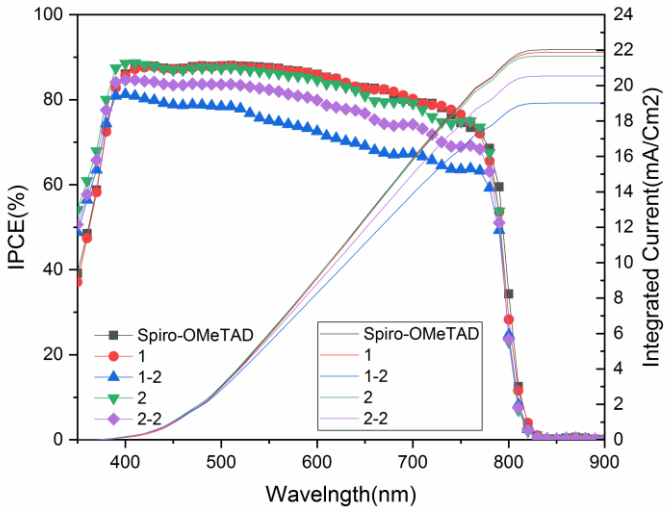

Figure 10. Incident photon-to-current efficiency (IPCE) curves for HTM.

Figure 11 shows the maximum power conversion efficiency as function of time from maximum power point tracking measurements under AM1.5 simulated solar light. These are initial values measured after device preparation and after 2 months of storing devices at dark in dry-box with humidity of less than 2% RH. The values are tabulated in **Table 6**. Maximum power point tracking (MMPT) for spiro-OMeTAD, **1** and **2-2** -based devices are 18.26, 15.08 and 15.33, respectively.

As a final and general comment, we observe that the trends observed in the PV performances of the studied compounds are at odds *wrt* the larger hole mobility of **1** in presence of additives as compared to both other compounds (**Figure 5**), thus pointing to other dominant factors. Additionally, these trends could hardly be related to differences in the corresponding HOMO levels, as the IP^{SS} or IP^{PES} values for **1** and **2** compounds vary by only 0.02 eV and by a maximum of only 0.04 eV with spiro-OMeTAD. Impact of the additives in the HTM layer morphology, or differences in interfacial properties could thus be in play, such as, amongst others, eventual energy level-shifts, the quality and strength of perovskite-HTM contact and interactions, polarity mismatch, etc.

Table 6. Maximum power point tracking (MPPT) for HTM devices for initial measurements and after 2 months.

HTMs	Spiro-OMeTAD	**1**	**1-2**	**2**	**2-2**
MPPT(%)	18.26	15.076	12.68	14.79	15.33
MPPT(%) After 2 month	17.93	15.01	------	14.43	-----

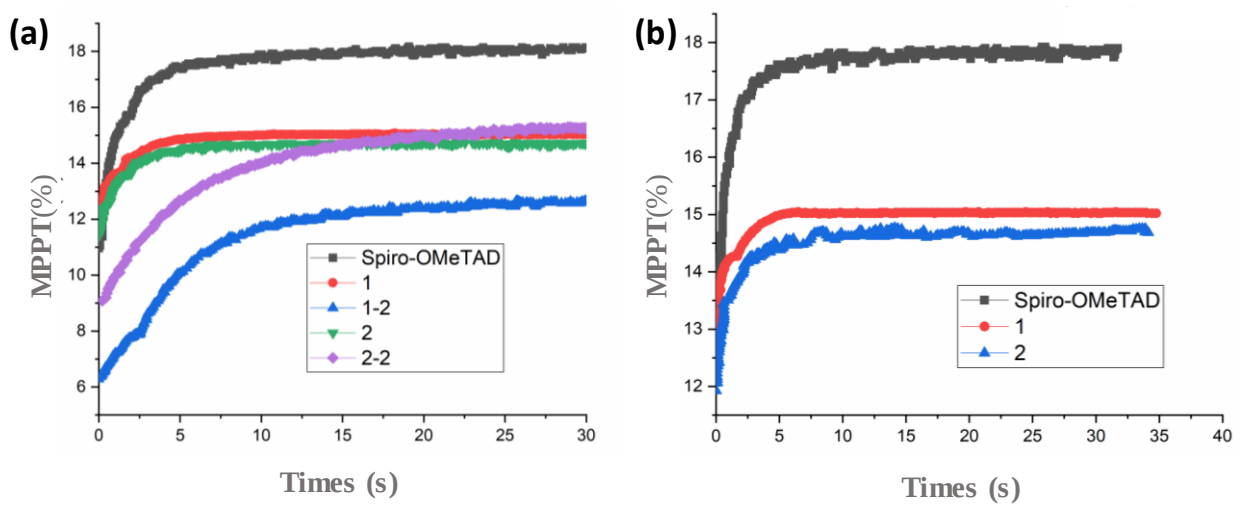

Figure 11. Maximum power conversion efficiency devices: (a) after device preparation (b) after 2 months.

4. Conclusions

The new spiro-MeTAD HTMs labelled as **1** and **2** were synthesized and applied in perovskite solar cells with the aim to outperform the spiro-OMeTAD based ones by means of improved hole mobility. Indeed, the results obtained for the pure HTM indicate stronger intermolecular interactions, smaller polarity, and larger hole mobility for **1** and **2** as compared to spiro-OMeTAD. However, the spiro-MeTAD-based PSC devices showed slightly inferior performances, with the best PCE of 17.2% and the lowest hysteresis obtained for **1**-based devices, as compared to 19.2% for spiro-OMeTAD -based devices. Given the better transport properties but slightly smaller performances of **1** and **2** compared to spiro-OMeTAD, these results comfort the idea that interface properties dominate the performances of PV devices in general as compared to HTM bulk properties. Our results suggest that the smaller PV performances of spiro-MeTAD compounds stem from less efficient perovskite → HTM hole transfer. The striking similarity of the new compounds with regard to the molecular shape, frontier orbital space-distribution, and energy levels of spiro-OMeTAD allows highlighting the dominant impact of the nature of the terminal groups (methyl versus methoxy) in the interaction between HTM-perovskite layers at their interface.

The influence of additive concentration in the HTM on the perovskite solar cell performance was investigated and showed important differences between the spiro-MeTAD- versus spiro-OMeTAD-based perovskite solar cells. Results showed that for **2-2**- based devices, efficiency reached to 18.0% in comparison with PCE of 19.2% in spiro-OMeTAD devices, but increasing additives concentration has a negative effect on hysteresis. Accordingly, the inclusion of additives in HTMs using the new spiro-MeTAD compounds would need further and careful optimization. As such, the similarity of PV performances of the new spiro-MeTAD compounds *wrt* spiro-OMeTAD suggests promising PV properties for these methylated spiro compounds, which could become even more attractive if their lower laboratory cost as compared to spiro-OMeTAD were to be similarly observed at the industrial level. Larger light transparency found for the new compounds and higher

glass transition temperatures in the case of compound 2 as compared to spiro-OMeTAD could additionally constitute valuable advantages for their use in perovskite solar cells.

ASSOCIATED CONTENT

Supporting Information. Results from time of flight (TOF) hole-mobility measurements at room temperature and as a function of temperature.

AUTHOR INFORMATION

Corresponding Authors:

E-mail: gjergji.sini@u-cergy.fr

E-mail: anders.hagfeldt@epfl.ch

E-mail: mortezaali@alzahra.ac.ir

ACKNOWLEDGMENT

M.S. acknowledges the Ministry of Science, Research and Technology of Iran for financial support. Zaiwei and Wang, Anand Agarwalla and Dr. Jingshan Luo at EPFL are acknowledged for experimental help. G.S. acknowledges the calculation centre of Cergy-Pontoise University for the computer time and support. D.V. acknowledges the Research Council of Lithuania (Project "OWEX", No S-MIP-17-101).

References

1. K. Kakiage, Y. Aoyama, T. Yano, K. Oya, J.-i. Fujisawa and M. Hanaya, *Chemical Communications*, 2015, **51**, 15894-15897.
2. , NREL PV EFFICIENCY CHART.
3. T. Leijtens, I. K. Ding, T. Giovenzana, J. T. Bloking, M. D. McGehee and A. Sellinger, *Acs Nano*, 2012, **6**, 1455-1462.
4. Y. Li, H. Li, C. Zhong, G. Sini and J.-L. Brédas, *npj Flexible Electronics*, 2017, **1**, 2.
5. X. Q. Jiang, D. P. Wang, Z. Yu, W. Y. Ma, H. B. Li, X. C. Yang, F. Liu, A. Hagfeldt and L. C. Sun, *Advanced Energy Materials*, 2019, **9**.

6. X. J. Ma, X. D. Zhu, K. L. Wang, F. Igbari, Y. Yuan, Y. Zhang, C. H. Gao, Z. Q. Jiang, Z. K. Wang and L. S. Liao, *Nano Energy*, 2019, **63**.
7. X. D. Zhu, X. J. Ma, Y. K. Wang, Y. Li, C. H. Gao, Z. K. Wang, Z. Q. Jiang and L. S. Liao, *Advanced Functional Materials*, 2019, **29**.
8. D. Alberga, G. F. Mangiatordi, F. Labat, I. Ciofini, O. Nicolotti, G. Lattanzi and C. Adamo, *Journal of Physical Chemistry C*, 2015, **119**, 23890-23898.
9. P. M. Borsenberger and H. Bassler, *Journal of Chemical Physics*, 1991, **95**, 5327-5331.
10. P. M. Borsenberger, W. T. Gruenbaum, E. H. Magin and L. J. Sorriero, *Chemical Physics*, 1995, **195**, 435-442.
11. P. M. Borsenberger, E. H. Magin, M. B. Oregan and J. A. Sinicropi, *Journal of Polymer Science Part B-Polymer Physics*, 1996, **34**, 317-323.
12. P. M. Borsenberger and L. B. Schein, *Journal of Physical Chemistry*, 1994, **98**, 233-239.
13. J. L. Maldonado, M. Bishop, C. Fuentes-Hernandez, P. Caron, B. Domercq, Y. D. Zhang, S. Barlow, S. Thayumanavan, M. Malagoli, J. L. Bredas, S. R. Marder and B. Kippelen, *Chemistry of Materials*, 2003, **15**, 994-999.
14. J. Keruckas, R. Lygaitis, J. Simokaitiene, J. V. Grazulevicius, V. Jankauskas and G. Sini, *Journal of Materials Chemistry*, 2012, **22**, 3015-3027.
15. D. Gudeika, J. V. Grazulevicius, G. Sini, A. Bucinskas, V. Jankauskas, A. Miasojedovas and S. Jursenas, *Dyes and Pigments*, 2014, **106**, 58-70.
16. V. Mimaite, J. V. Grazulevicius, R. Laurinaviciute, D. Volyniuk, V. Jankauskas and G. Sini, *Journal of Materials Chemistry C*, 2015, **3**, 11660-11674.
17. D. Gudeika, J. V. Grazulevicius, D. Volyniuk, G. Juska, V. Jankauskas and G. Sini, *The Journal of Physical Chemistry C*, 2015, **119**, 28335-28346.
18. Y. Nakayama, S. Machida, D. Tsunami, Y. Kimura, M. Niwano, Y. Noguchi and H. Ishii, *Applied Physics Letters*, 2008, **92**, 153306.
19. A. Pivrikas, N. S. Sariciftci, G. Juška and R. Österbacka, *Progress in Photovoltaics: Research and Applications*, 2007, **15**, 677-696.
20. W. Kohn and L. J. Sham, *Phys. Rev.*, 1965, **140**, A1133-A1138.
21. A. D. Becke, *The Journal of Chemical Physics*, 1993, **98**, 5648-5652.
22. C. T. Lee, W. T. Yang and R. G. Parr, *Physical Review B*, 1988, **37**, 785-789.
23. J. D. Chai and M. Head-Gordon, *Phys. Chem. Chem. Phys.*, 2008, **10**, 6615-6620.
24. E. K. U. Gross and W. Kohn, *Phys. Rev. Lett.*, 1985, **55**, 2850-2852.
25. E. K. U. Gross and W. Kohn, *Adv. Quant. Chem.*, 1990, **21**, 255-291.
26. M. E. Casida, C. Jamorski, K. C. Casida and D. R. Salahub, *Journal of Chemical Physics*, 1998, **108**, 4439-4449.
27. E. Runge and E. K. U. Gross, *Adv. Quant. Chem.*, 1984, **21**, 255.
28. R. Bauernschmitt and R. Ahlrichs, *Chemical Physics Letters*, 1996, **256**, 454-464.
29. D. Beljonne, J. Cornil, L. Muccioli, C. Zannoni, J.-L. Bredas and F. Castet, *Chemistry of Materials*, 2011, **23**, 591-609.
30. E. F. Valeev, V. Coropceanu, D. A. da Silva Filho, S. Salman and J.-L. Bredas, *Journal of the American Chemical Society*, 2006, **128**, 9882-9886.
31. M. J. Frisch, G. W. Trucks, H. B. Schlegel, G. E. Scuseria, M. A. Robb, J. R. Cheeseman, G. Scalmani, V. Barone, B. Mennucci, G. A. Petersson, H. Nakatsuji, M. Caricato, X. Li, H. P. Hratchian, A. F. Izmaylov, J. Bloino, G. Zheng, J. L. Sonnenberg, M. Hada, M. Ehara, K. Toyota, R. Fukuda, J. Hasegawa, M. Ishida, T. Nakajima, Y. Honda, O. Kitao, H. Nakai, T. Vreven, J. Montgomery, J. A., J. E. Peralta, F. Ogliaro, M. Bearpark, J. J. Heyd, E. Brothers, K. N. Kudin, V. N. Staroverov, T. Keith, R. Kobayashi, J. Normand, K. Raghavachari, A. Rendell, J. C. Burant, S. S. Iyengar, J. Tomasi, M. Cossi, N. Rega, J. M. Millam, M. Klene, J. E. Knox, J. B. Cross, V. Bakken, C. Adamo, J. Jaramillo, R. Gomperts, R. E. Stratmann, O. Yazyev, A. J. Austin, R. Cammi, C. Pomelli, J. W. Ochterski, R. L. Martin, K.

Morokuma, V. G. Zakrzewski, G. A. Voth, P. Salvador, J. J. Dannenberg, S. Dapprich, A. D. Daniels, O. Farkas, J. B. Foresman, J. V. Ortiz, J. Cioslowski and D. J. Fox, 2009, **Gaussian 09, Revision B.01, Gaussian Inc., Wallingford CT, 2010..**
32. Z. Hawash, L. K. Ono and Y. Qi, *Advanced Materials Interfaces*, 2018, **5**, 1700623.
33. N. Arora, M. I. Dar, A. Hinderhofer, N. Pellet, F. Schreiber, S. M. Zakeeruddin and M. Grätzel, *Science*, 2017, **358**, 768.
34. B. Xu, E. Sheibani, P. Liu, J. Zhang, H. Tian, N. Vlachopoulos, G. Boschloo, L. Kloo, A. Hagfeldt and L. Sun, *Advanced Materials*, 2014, **26**, 6629-6634.
35. D. Shi, X. Qin, Y. Li, Y. He, C. Zhong, J. Pan, H. L. Dong, W. Xu, T. Li, W. P. Hu, J. L. Bredas and O. M. Bakr, *Science Advances*, 2016, **2**.
36. H. Bassler, *Physica Status Solidi B-Basic Research*, 1993, **175**, 15-56.
37. D. Bi, B. Xu, P. Gao, L. Sun, M. Grätzel and A. Hagfeldt, *Nano Energy*, 2016, **23**, 138-144.

TOC

Two new spiro-**Me**TAD (**1** and **2**) Hole Transporting Materials were synthesized and applied in perovskite solar cells with the aim to outperform spiro-**OMe**TAD. Despite larger hole mobilities, smaller PCE were obtained for spiro-**Me**TAD as compared to spiro-**OMe**TAD, stemming from less efficient perovskite→HTM hole transfer. These results alert on the necessity to **give priority to improving perovskite-HTM interaction properties.**